Exclusive studies of 130–270 MeV ^{3}He- and 200-MeV proton-induced reactions on ^{27}Al, ^{nat}Ag, and ^{197}Au

D. S. Ginger,[*] K. Kwiatkowski,[†] G. Wang,[‡] W.-c. Hsi,[§] S. Hudan, E. Cornell,[‖] R. T. de Souza, and V. E. Viola
Department of Chemistry and IUCF, Indiana University, Bloomington, Indiana 47405, USA

R. G. Korteling
Department of Chemistry, Simon Fraser University, Burnaby, British Columbia, Canada V5A I56
(Received 30 November 2007; published 2 September 2008)

Exclusive light-charged-particle and IMF spectra have been measured with the ISiS detector array for bombardments of ^{27}Al, ^{nat}Ag, and ^{197}Au nuclei with 130–270-MeV ^{3}He and 200-MeV protons. The results are consistent with previous interpretations based on inclusive data that describe the global yield of complex fragments in terms of a time-dependent process. The emission mechanism for energetic nonequilibrium fragments observed at forward angles with momenta up to twice the beam momentum is also investigated. This poorly understood mechanism, for which the angular distributions indicate formation on a time scale comparable to the nuclear transit time, are accompanied primarily by thermal-like emissions. The data are most consistent with a schematic picture in which nonequilibrium fragments are formed in a localized region of the target nucleus at an early stage in the energy-dissipation process, where the combined effects of high energy density and Fermi motion produce the observed suprathermal spectra.

DOI: 10.1103/PhysRevC.78.034601 PACS number(s): 25.55.−e, 25.40.Sc, 25.70.Mn

I. INTRODUCTION

Among the most poorly-understood phenomena observed in collisions between intermediate-energy projectiles and complex nuclei is the formation of fast, forward-peaked intermediate-mass fragments (IMF: $3 \leqslant Z \lesssim 15$). These fragments are most transparently distinguished from equilibrium-like processes in reactions induced by H and He projectiles with energies between 100–1000 MeV [1] and reviewed in [2]. They are also an important component of the yield in heavy-ion reactions [2,3]. Experimentally, nonequilibrium emission is characterized by strongly forward-peaked angular distributions, indicating a fragment formation time of $\lesssim$30 fm/c. Further, the Maxwellian spectra exhibit hard tails that have slope temperatures 2–3 times those expected for a complete-fusion residue and extend up to momenta in excess of twice the beam momentum [4,5]. This latter observation suggests the importance of a fast collective mechanism in which Fermi momentum plays an important role.

In contrast, at bombarding energies in the vicinity of the barrier, it has been shown that IMF emission is an evaporative process controlled by ℓ-dependent barriers and the excitation energy of the system [6,7]. In this energy regime the IMF spectra are Maxwellian in shape, peaking near the Coulomb barrier, and exhibit slopes consistent with the binary decay of an equilibrated composite nucleus. Several theoretical treatments have successfully modeled these events within a statistical formalism [2,8,9].

At beam energies above a few GeV, multiple IMF emission, or multifragmentation, becomes a significant additional mechanism for IMF production. IMF spectra from light-ion-induced reactions are characterized by unusually low average kinetic energies, presumably due to the expansion/dilution of the hot source [10]. As in the case of nonequilibrium emission below the multifragmentation threshold, fragment formation occurs on a fast timescale as projectile kinetic energy is dissipated into internal excitation of the system [11]. Intranuclear cascade [12–14] and BUU [15,16] approaches account for the initial projectile-target interaction relatively well, and the final state of these hot systems can be well described by statistical models [17–19]. However, attempts to couple transport and decay phenomena in order to describe the full evolution of these systems have met with only limited success. Thus, the development of a unified reaction model for multifragmentation poses a complex theoretical challenge.

The case of nonequilibrium IMF emission in light-ion-induced reactions presents perhaps the simplest case for investigating dynamic fragment formation during the dissipative phase of these reactions. Light-charged-particle (LCP: H and He isotopes) emission has been accounted for by preequilibrium [20–22] and coalescence [23] models. However, these approaches do not include IMF emission. Attempts to deal specifically with the question of complex fragment production have included the "snowball" model of Boal [24] and the expanding accreting source model of Fields *et al.* [25]. Both of these models invoke the concept of a localized region of high excitation to produce energetic IMFs and have been able to describe some aspects of the data [4,5,26].

[*]Present address: Department of Chemistry, University of Washington, Seattle, WA 98467.
[†]Present address: Physics Division, Los Alamos National Laboratory, Los Alamos, NM 87545.
[‡]Present address: Epsilon Corp., Irving, TX 75063.
[§]Present address: Midwest Proton Radiation Institute, Indiana University, Bloomington, IN 47408.
[‖]Present address: Lawrence Berkeley Laboratory, Berkeley, CA 94720.

The objective of the present research has been to study nonequilibrium emission in the Fermi-energy regime in an effort to gain greater experimental insight into this phenomenon. The experiment described here is the first attempt to use a high solid angle multiple detector array to study such reactions, thus permitting examination of correlations among various reaction observables. We first describe the experimental arrangement and then discuss the implications of the data on the understanding of these processes.

II. EXPERIMENTAL DETAILS

A. Apparatus

The experiment was performed at the Indiana University Cyclotron facility with the Indiana Silicon Sphere (ISiS) detector array [27]. Beams of 130- and 270-MeV ^{3}He and 200-MeV protons bombarded targets of ^{27}Al, ^{nat}Ag, and ^{197}Au. The data presented here are primarily for the ^{nat}Ag target, for which statistics were the highest. The ISiS array [27] consists of 162 triple detector telescopes arranged in a spherical geometry. Angular acceptance is 14°–86.5° in the forward hemisphere and 93.5°–166° at backward angles, with a total solid- angle coverage of 74% of 4π. Each telescope includes a gas-ionization counter (IC) operated with C_3F_8 gas, a 500-μm ion-implanted silicon (Si) detector and a 28 -mm-thick CsI crystal with photodiode readout. The telescopes provide Z-identification for fragments with $Z < 16$ and energies $0.7 \leqslant E/A \leqslant 8$ MeV and isotope identification for $8 \leqslant E/A \leqslant 92$ MeV fragments, primarily $Z = 1$–4 in this experiment. The target thicknesses for the ^{3}He runs were 1.05 mg/cm^2 ^{197}Au, and 0.68 mg/cm^2 ^{nat}Ag; the target thicknesses for the proton runs were 1.08 mg/cm^2 ^{197}Au, 0.62 mg/cm ^{nat}Ag, and 0.20 mg/cm^2 ^{27}Al.

During all runs the ISiS hardware trigger logic for event acceptance was set for valid coincident signals in two or more of the 162 silicon detectors. Following a valid trigger, the IC/Si/CsI ADC's were read out for each detector that had a fast silicon signal passing the discriminator threshold. In order to detect highly energetic light ions, the data-acquisition code also checked the ADC hit registers for all CsI detectors whenever an ISiS event occurred. During the ^{3}He runs, if a CsI detector fired without its corresponding silicon, then that CsI ADC was also read and included in the event file. Gas pressure in each ISiS hemisphere was monitored remotely. The average forward hemisphere gas pressure was 17.7 ± 0.3 Torr, during the ^{3}He runs, and 18.03 ± 0.15 Torr during the proton runs. The average backward hemisphere pressure was 18.8 ± 0.3 Torr during the ^{3}He runs, and 16.62 ± 0.24 Torr during the proton runs.

B. Detector calibrations

The silicon detectors were calibrated with an Ortec precision pulser and an ^{241}Am alpha calibration source and a precision pulser. The data from the test-input linearity checks showed the detector and electronics response to be well described by a single linear fit. To check the accuracy of the silicon absolute energy calibration, the proton and alpha-particle punch-through energies for each detector were calculated with the DONNA energy loss program [28] and the manufacturer-supplied thicknesses of the silicon detectors. In most cases the predicted and observed values were found to agree within better than 1% for both proton- and alpha-particle punch-throughs for the silicon detectors. The linearity of the electronics for the gas-ionization chambers was checked by a method analogous to that used with the silicon detectors. Once linear response had been confirmed, absolute energies for the gas-ionization chambers (IC's) were established through cross calibration against the silicon energies. The CsI(Tl) crystals were calibrated in a manner similar to that of the gas-ionization chambers. However, because of the light output of a CsI(Tl) crystal varies as a function of particle type and energy [29,30], separate calibrations were performed for the proton, deuteron, triton, ^{3}He, ^{4}He, ^{6}Li, and ^{7}Li lines in the silicon vs. CsI(Tl) spectra. Losses in the silicon dead layer and aluminized-mylar crystal wrapping were accounted for.

The elastic-scattering peak of the 130-MeV ^{3}He beam was well defined in the most forward CsI ring and was used as a check of the calibration accuracy. The agreement indicates that the CsI calibration is accurate to within 2%. Further details of the calibration procedures can be found in [31].

III. RESULTS

Previous inclusive studies of light-ion-induced reactions in the Fermi-energy domain have shown that LCP and IMF production occur from two principal mechanisms: statistical decay of an equilibrated residue and fast nonequilibrium emission. The equilibrium component is supported by the observation of nearly isotropic angular distributions for the heavier fragments and Maxwellian spectra with slope temperatures consistent with evaporation from a composite nucleus. The nonequilibrium events are strongly forward peaked and exhibit spectral tails that extend to kinetic energies much greater than expected for compound nucleus decay. Semi-exclusive studies [32–34] have shown that the equilibrium IMFs appear to originate in more central collisions whereas nonequilibrium events come from peripheral processes. In addition, LCP-LCP correlation studies [35] indicate that nonequilibrium emission occurs from a smaller, hotter source than equilibrium emission.

A. Inclusive results

In Fig. 1 we show representative inclusive ^{4}He energy spectra as a function of angle for the 200-MeV $p + ^{nat}$Ag reaction. Both the spectral shapes and their angular evolution are typical of the combined effects of equilibrium and nonequilibrium emission and are in good agreement with previous measurements [1]. The Coulomb-like spectral peaks evolve systematically with angle and exhibit angular distributions that are approximately isotropic. The high-energy tails of the ^{4}He spectra, however, extend up to about 170 MeV, nearly twice the momentum of the beam. While the strong bias for forward angles is apparent for the nonequilibrium events, it is observed that these tails persist even at the backward-most angles.

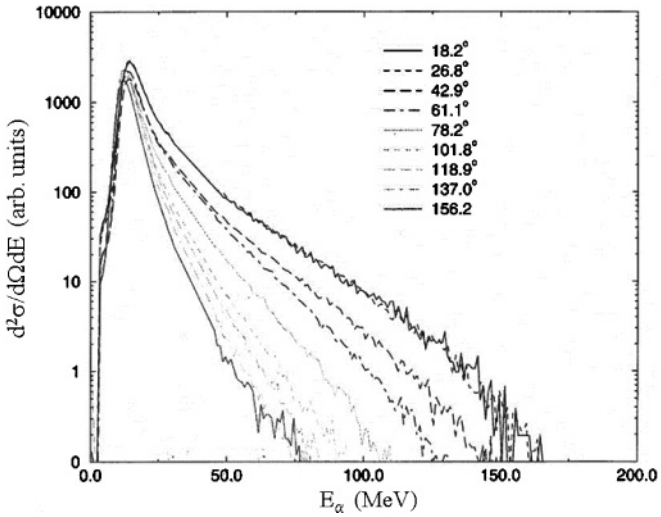

FIG. 1. Alpha particle spectra at all measured angles for the 200-MeV $p + ^{nat}$Ag reaction in coincidence with one or more charged particles.

Although the cross section for these events is small, their explanation nonetheless constitutes a significant challenge for theory.

The laboratory angular distributions for the integrated spectra, shown in Fig. 2 for $Z = 1$–9 nuclei emitted in the 200-MeV $p + ^{nat}$Ag reaction, also exhibit characteristic behavior, i.e., the yield is peaked along the beam direction in the forward hemisphere, but nearly isotropic for angles greater than 90°. This behavior is observed for the other systems studied here as well. The forward peaking is strongly influenced by the energetic tails of the spectra. This is illustrated in Fig. 3 where laboratory angular distributions are plotted for evaporation protons in the spectral peaks ($E_p < 12$ MeV) and the nonequilibrium tails ($E_p > 20$ MeV). Whereas the evaporative component is consistent with isotropic emission from a slowly moving source (velocity $< 0.01c$), the observed

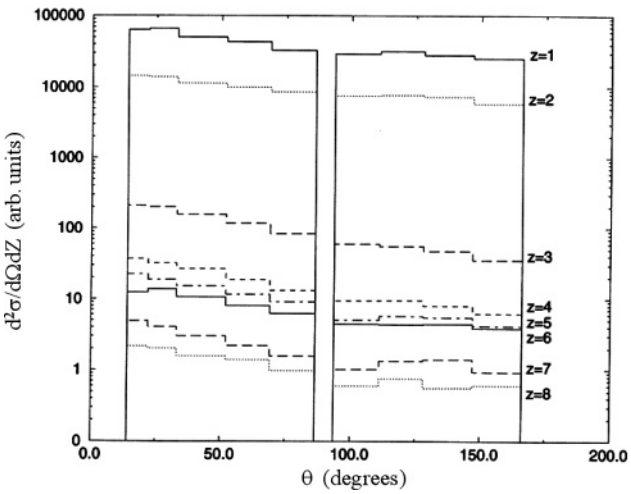

FIG. 2. Angular distributions for $Z = 1$–9 fragments for the 200-MeV $p + ^{nat}$Ag reaction in coincidence with one or more charged particles.

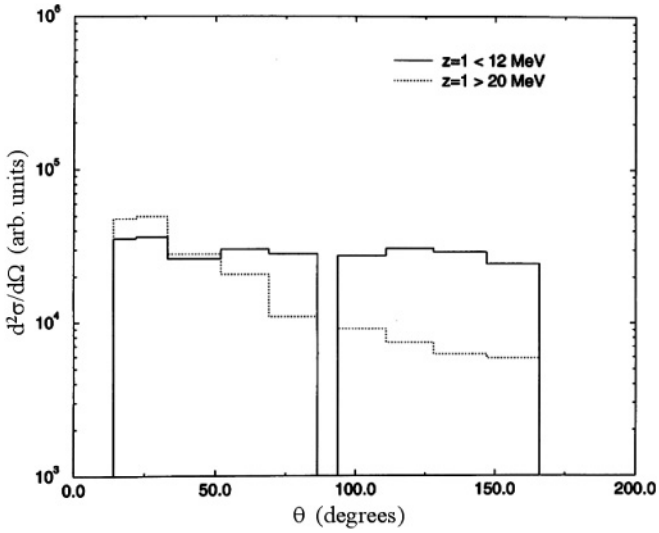

FIG. 3. Angular distribution of evaporative ($E_p < 12$ MeV) and nonequilibrium ($E_p > 12$ MeV) $Z = 1$ fragments for the 200-MeV $p + ^{nat}$Ag reaction in coincidence with one or more charged particles.

nonequilibrium yield increases by an order of magnitude between the most backward and most forward angles. For the heavier fragments the forward-backward ratios are of order three-to-four, except for He ions for which a much flatter angular distribution is observed relative to IMFs. This difference may be due to the large yield of ^{4}He from secondary decay of heavier fragments in addition to the residue.

Two other features of the inclusive data also are consistent with earlier data: the charge distributions and the ^{3}He/^{4}He isotope ratio. The charge distribution for the 200-MeV $p + ^{nat}$Ag reaction is shown in Fig. 4. Power-law and exponential fits to the charge distributions (including He) yield exponent

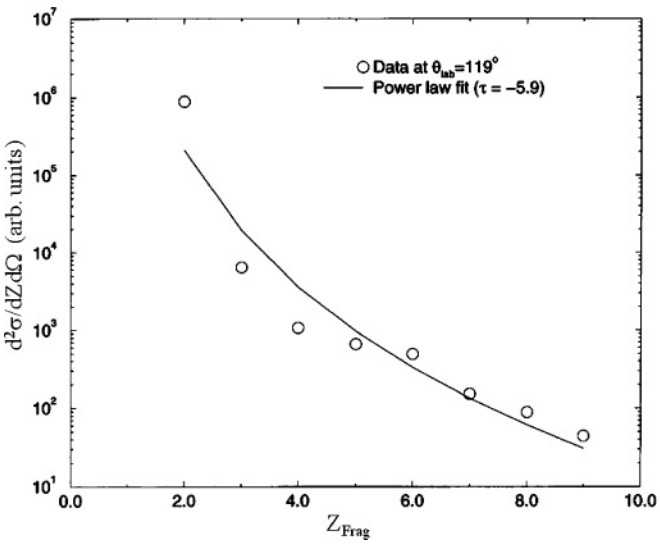

FIG. 4. Fragment charge distribution for the 200-MeV $p + ^{nat}$Ag reaction measured at 119 degrees in the laboratory frame in coincidence with one or more charged particles. Circles are data, the line represents a power-law fit to the cross sections (including He) with exponent $\tau \sim -5$.

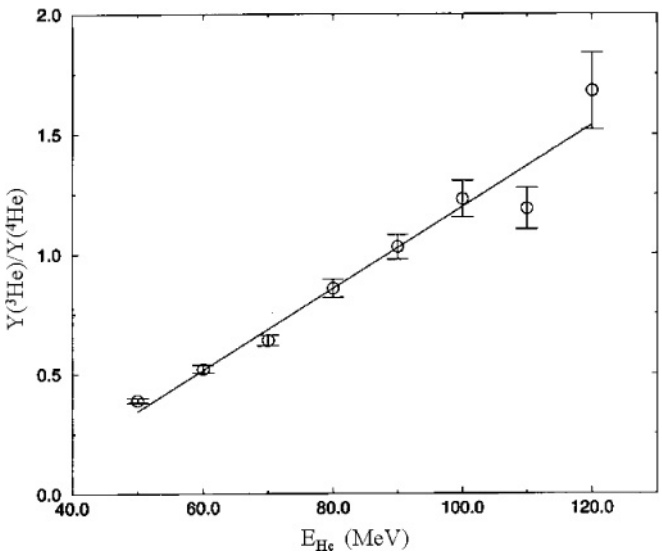

FIG. 5. Ratio of ^{3}He-to-^{4}He yield as a function of He energy, measured at 18 degrees in the laboratory frame for the 200-MeV $p + {}^{\text{nat}}$Ag reaction. Circles represent data, error bars correspond to one standard deviation due to random error, the straight line is a linear fit to the data.

values of order 4–5 for the various systems studied here. Figure 5 presents the ratio of ^{3}He to ^{4}He as a function of energy measured at 18° in the laboratory system for 200-MeV protons incident on $^{\text{nat}}$Ag. The ^{3}He/^{4}He dependence on He kinetic energy measured here is nearly identical to that observed with 4.8 GeV ^{3}He-ion bombardments of $^{\text{nat}}$Ag and ^{197}Au [36]. In the present case the spectra strongly support an interpretation in which evaporative ^{4}He ions dominate the ratio at low He kinetic energies, but as the He energy increases, the nonequilibrium tail of the ^{3}He spectrum becomes the principal isotopic species, as has previously been reported [37,38].

B. Exclusive results

Since these measurements comprise the first light-ion study at these bombarding energies in which charged particles have been detected with large solid-angle coverage, broad fragment energy acceptance and significant detector granularity, they provide a unique opportunity to utilize coincidence gates and particle-correlation techniques to characterize the reaction mechanism(s).

1. Multiplicity distributions

One useful gauge of excitation-energy deposition in intermediate-to-high energy collisions is the charged-particle multiplicity (N_{CP}) distribution. Here we identify (N_{CP}) as the number of observed charged particles in an event, to be distinguished from the true multiplicity, M, corrected for detector acceptance.

Figure 6 summarizes the observed multiplicity distributions for ^{3}He bombardment of $^{\text{nat}}$Ag and ^{197}Au targets. Plots are normalized so that $N_i/N_{\text{tot}} = 1$. The left-hand panel shows

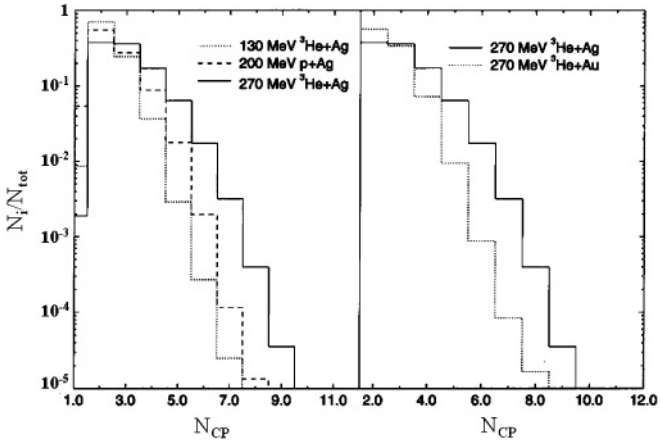

FIG. 6. Charged particle multiplicity distributions for the ^{3}He + $^{\text{nat}}$Ag and ^{3}He + ^{197}Au reactions, at energies indicated. Each histogram is normalized so that $N_i/N_{\text{tot}} = 1$.

the influence of light-ion bombarding energy for the $^{\text{nat}}$Ag target. Up to nine charged particles are detected in the most violent events and the dependence on total projectile energy is apparent in the figure. Thus, the qualitative correlation with expected energy deposition is confirmed. In order to reconstruct the total excitation energy deposition E^*, it is necessary to account for neutron emission. However, no neutron-charged particle correlation measurements currently exist for similar reactions so that any such reconstruction would be highly model-dependent.

The right-hand panel of Fig. 6 compares the observed multiplicity distributions for the same projectile and bombarding energy with 270-MeV ^{3}He ions incident on $^{\text{nat}}$Ag and ^{197}Au targets. The higher values of N_{CP} for the $^{\text{nat}}$Ag target are attributed to two factors. First, neutrons compete more favorably with charged-particle emission for the higher Z, more neutron rich, ^{197}Au nucleus, and second, higher E^*/A values (temperatures) should be reached with the $^{\text{nat}}$Ag nuclei relative to ^{197}Au, thus reducing the Coulomb barrier hindrance to charged-particle emission.

Next we consider the influence of various coincidence gates on the multiplicity distributions. Figures 7 and 8 compare multiplicity distributions for the 270-MeV ^{3}He + $^{\text{nat}}$Ag and the 200-MeV $p + {}^{\text{nat}}$Ag systems, respectively. In each figure N_{CP} distributions are shown for all events (dominated by p and ^{4}He) and events containing at least one IMF. By requiring coincidence with an IMF, the distribution is skewed towards higher multiplicities for both projectile types. If N_{CP} is again used as a gauge of excitation energy, these figures suggest that on average IMF emission is associated with higher excitation energy deposition in the collision. In addition, Fig. 7 shows the multiplicity distribution associated with events containing a Li fragment with a kinetic energy above 90 MeV (85% of the ^{3}He beam momentum). For this gate, it is observed that the chance of an event with a high multiplicity decreases by nearly an order of magnitude. This fact highlights the sensitivity of the coincidence measurements to the finite energy available in the system: ejection of a highly energetic particle leaves behind a proportionately cooler residue that is less capable

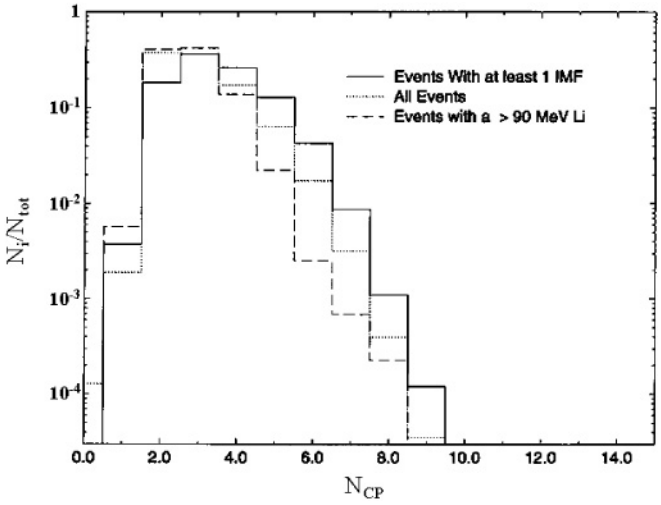

FIG. 7. Charged-particle multiplicity distributions for the 270-MeV ^{3}He + ^{nat}Ag system under three gating conditions: (1) events containing at least one IMF, (2) all events, and (3) events with a high energy Li(>90 MeV). Each histogram is normalized so that $\Sigma N_i/N_{tot} = 1$.

of emitting large numbers of particles. The high energy Li fragments are strongly forward-peaked and would generally be attributed to nonequilibrium-like processes. The contrast between the two IMF gates leads one to speculate that gating on equilibrium-like IMFs may serve as a centrality gauge for these reactions (indeed, the best theoretical fits to the backward angle fragment charge distributions in Ref. [5] assumed full linear momentum transfer).

The angular distributions of fragments observed in coincidence with an IMF are presented in Fig. 9 for the 200-MeV $p + ^{nat}$Ag reaction. Relative to the inclusive data presented in Fig. 2, there is a strong suppression of forward-peaked LCPs

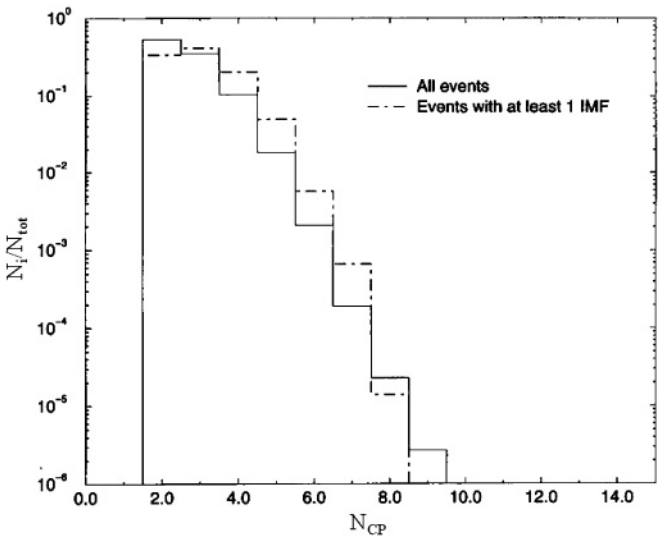

FIG. 8. Charged-particle multiplicity distributions for the 200-MeV $p + ^{nat}$Ag reaction under two gating conditions: (1) all events and (2) events with at least one IMF. Each histogram is normalized so that $\Sigma N_i/N_{tot} = 1$.

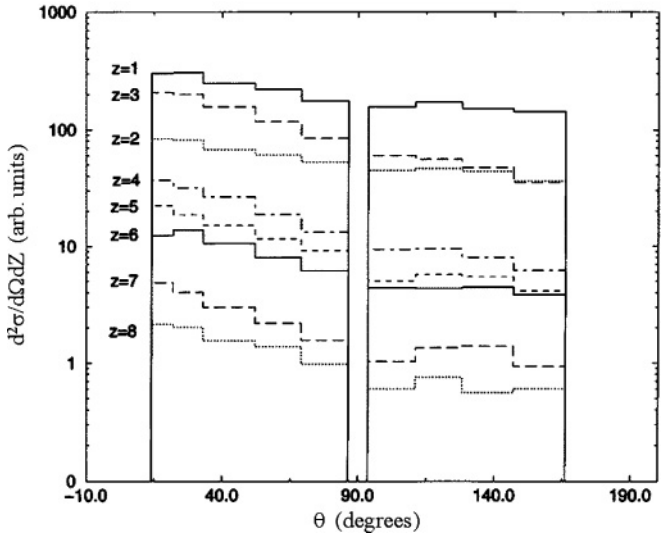

FIG. 9. Angular distributions for fragments observed in events containing at least one IMF. Progression in order of relative cross section proceeds $Z = 1, 3, 2, 4, 5, 6, 7, 8$.

relative to IMFs when demanding coincidence with a larger fragment. This is consistent with energy conservation considerations associated with emitting an IMF, as discussed above. However, it should be remembered that these IMF events still have higher charged-particle multiplicities than average inclusive events (Fig. 8). While somewhat counterintuitive, these trends are consistent: the lower average multiplicities observed for all events is due to the large weight of $N_{CP} = 2$ events in the average and events consisting only of $Z = 1$ and $Z = 2$ fragments, which drive down the relative probabilities of higher N_{CP} events.

2. Linear momentum distributions

Linear momentum distributions were used to investigate the formation of non- equilibrium IMFs. Figure 10 shows the distribution of total observed linear momentum for events with a fast, forward Li fragment ($E_{Li} > 50$ MeV, $14^\circ \leqslant \theta_{lab} \leqslant 33^\circ$) emitted in the 200 MeV $p + ^{nat}$Ag reaction. The broad distribution extends past twice the beam momentum of 640 MeV/c and peaks around 950 MeV/c, indicating that a large amount of unobserved momentum was carried away in the backward direction. In Fig. 11 the event-by-event total transverse momentum distributions observed for events with the fast, forward fragments ($E_{Li} > 50$ MeV, $14^\circ \leqslant \theta_{lab} \leqslant 33^\circ$) (right frame), is compared with the transverse momentum distribution observed for all events (left frame). It is seen that, in general, the events containing preequilibrium Li fragments appear to have a much more diffuse "doughnut-like" distribution, corresponding to the transverse projection of the fast Li momenta at the gated angles. This fact, along with the large amount of "missing" backward linear momentum in Fig. 10 indicates that the unobserved transverse momentum is carried away in a direction opposite that of the preequilibrium Li fragment.

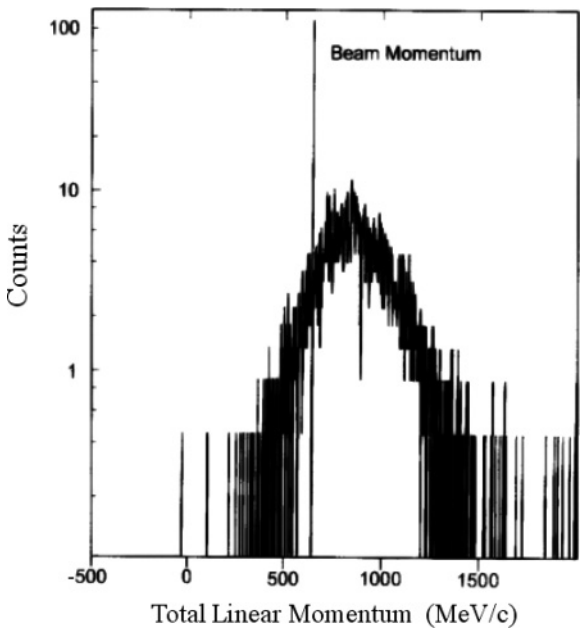

FIG. 10. Total linear momentum for 200-MeV $p + {}^{\text{nat}}\text{Ag}$ events with a fast forward Li. ($E_{\text{Li}} > 50$ MeV, $14^\circ \leqslant \theta \leqslant 33^\circ$). The impulse at 644 MeV/c indicates the beam momentum.

Because of the high energy acceptance of the ISiS array, it is extremely unlikely that the missing momentum is carried away by light charged particles or IMFs. We therefore deduce that the undetected momentum balance is accounted for by the recoil of the heavy residue (which would fall below the ISiS E/A acceptance). Such a conclusion is consistent with an intermediate time-scale process (such as an accreting source or coalescence-like ejection) as has been suggested previously [4,5].

We have also examined the total charge and momentum balance in the 200 MeV $p+{}^{27}\text{Al}$ reaction. As the left frame of Fig. 12 shows, there are a large number of events for which the entire charge of the system is observed for the ^{27}Al target, (the available E^*/A is ~ 7 MeV/nucleon, on the order of the total binding energy). The right-hand frame of Fig. 12 shows the total linear momentum detected for those events where nearly the entire charge of the system has been observed ($12 \leqslant Z_{\text{obs}} \leqslant 14$.). The momentum distribution peaks at 550 MeV/c, roughly 85% that of the beam, with a full-width at half-maximum of 430 MeV/c. The balance of the momentum is most likely carried by neutrons and the average one-to-two charged particles that are not observed due to geometry. The angle-dependent fragment-charge distributions for events falling into the $12 \leqslant Z_{\text{obs}} \leqslant 14$ gate (Fig. 13) are consistent with

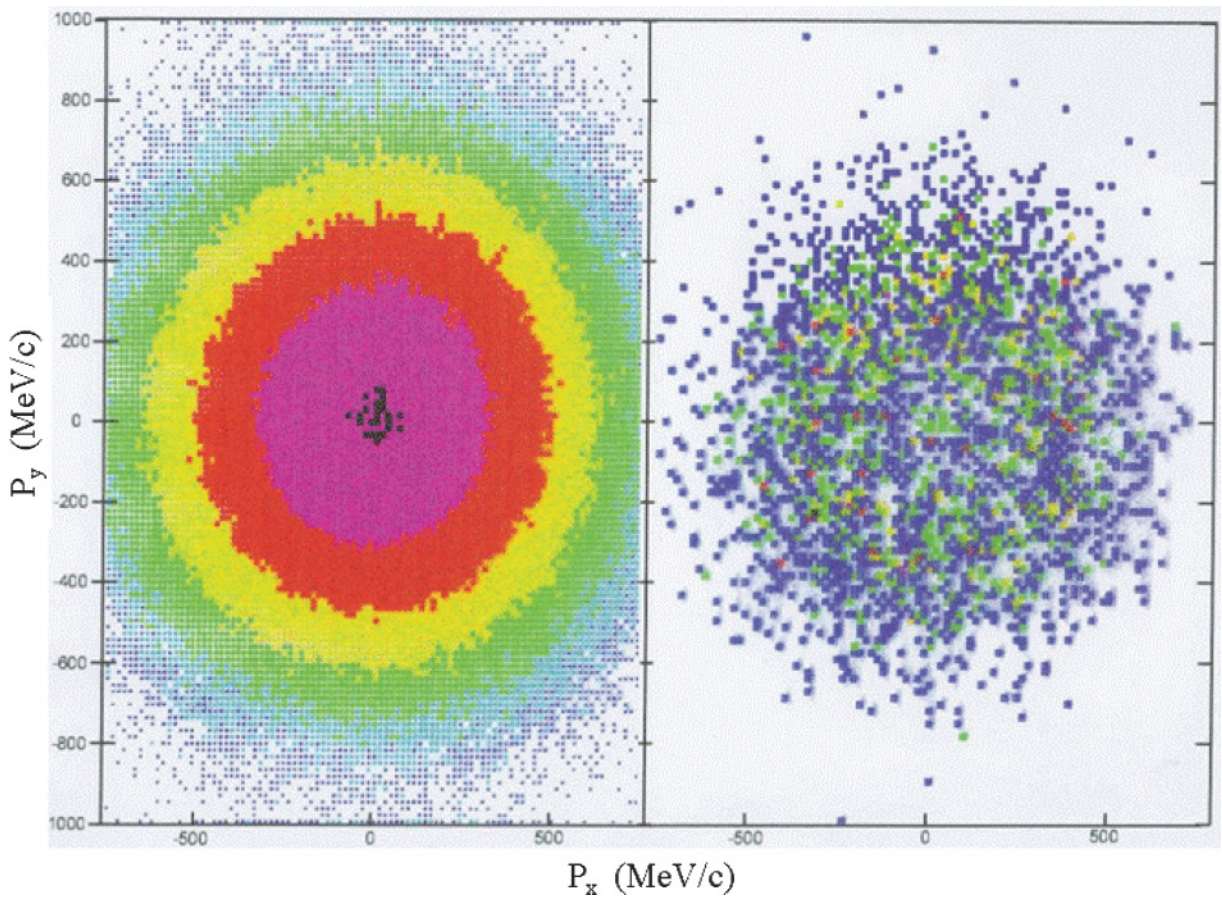

FIG. 11. (Color online). Transverse momentum distributions for all events (left frame) and events containing a fast forward Li (right frame), ($E_{\text{Li}} > 50$ MeV, $13^\circ \leqslant \theta \leqslant 33^\circ$), for the 200-MeV $p + {}^{\text{nat}}\text{Ag}$ reaction. Intensity color coding: black > purple > red > yellow > green > blue > violet.

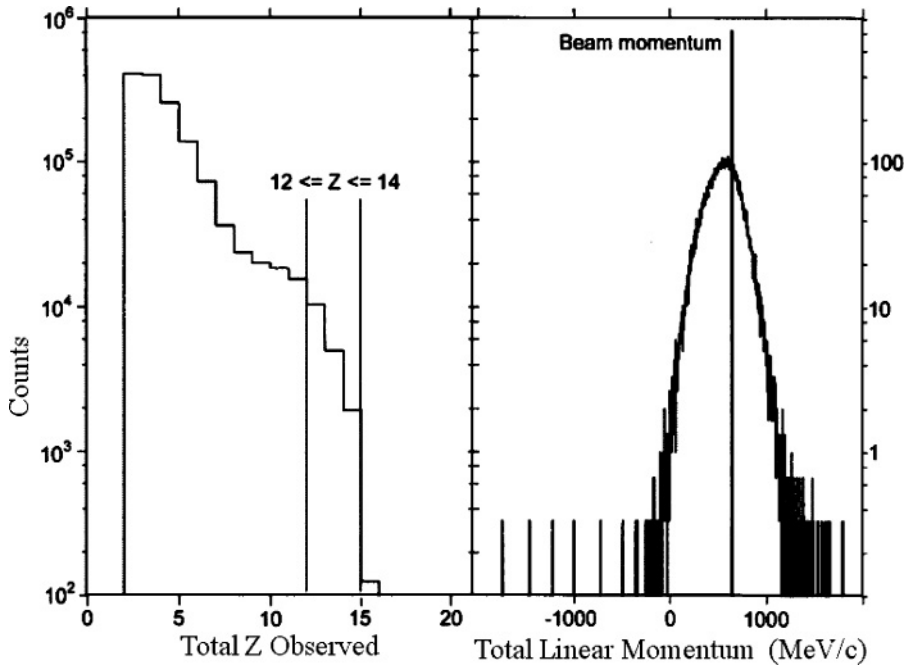

FIG. 12. Left frame: Distribution of total observed charge for valid 200-MeV $p + {}^{27}$Al events. Vertical lines indicate gating condition for right frame. Right frame: distribution of total linear momentum for those $p + {}^{27}$Al events for which $12 \geqslant Z_{\rm obs} \geqslant 14$. Impulse at 644 MeV/$c$ indicates beam momentum.

these high linear momentum transfers, showing an excess of heavier "residue-like" fragments at the forward lab angles, and more typical power-law-like behavior at backward lab angles.

3. *Fragment-fragment correlations*

If the forward peaking of the differential cross sections is due to preequilibrium emission, measurements of the forward-to-backward yield ratios under various gating conditions may provide information regarding the equilibrium and preequilibrium character of the reaction. Table I lists forward-to-backward yield ratios as a function of fragment charge observed under four gating conditions: (1) all events, (2) those events with an energetic backward proton ($E_p >$ 20 MeV, $147 \leqslant \theta_{\rm lab} \leqslant 166^\circ$), (3) those events with a lower energy backward proton ($9 \leqslant E_p \leqslant 12$ MeV, $147^\circ \leqslant \theta_{\rm lab} \leqslant 166^\circ$), and (4) those events with an energetic forward proton ($E_p >$ 20 MeV, $33^\circ \leqslant \theta_{\rm lab} \leqslant 52^\circ$). Autocorrelation due to gating on angles used in the ratio definitions was minimized by normalizing yields in the gated regions to the remainder of the spectrum.

The results show that the most forward-peaked distributions of LCPs and IMFs are obtained in coincidence with the energetic backward protons. The ratios become consistently more isotropic as one moves from the lower-energy backward protons, to the sum of all events, and finally showing the least forward peaking when coincidence with an energetic forward proton is required. For all gating conditions, Li fragments show the strongest forward peaking, and He fragments show the most isotropic distribution (consistent with the previous discussion of evaporation/preequilibrium yields). It is attractive to speculate on the source of the increased forward peaking observed for the backward-angle proton gates. However, it is not clear as yet whether the trend is due to a change in equilibrium and preequilibrium ratios, to an anti-correlation of fragment emission at angles near those of the gated particle, or simply to momentum-conservation effects. Any full explanation must account for the decreased anisotropy observed for the energetic-forward-proton gate.

Fragment-fragment correlation studies also provide insight into the breakup dynamics of these reactions. In Fig. 14, the correlation functions for the opening angle between two complex fragments are shown for the 200-MeV $p+{}^{27}$Al and ${}^{\rm nat}$Ag systems. The angular correlation function is defined as:

$$R(\theta) + 1 = \sum_{ij} Y_{ij}(\theta_{ij}\theta_j) \Big/ \sum_{kl} Y_{\rm mix}(\theta_k, \theta_l) \qquad (1)$$

where Y_{ij} refers to two fragments in the same event emitted at angles i and j, and $Y_{\rm mix}$ selects fragments from two separate

TABLE I. Forward ($14^\circ \leqslant \theta_{\rm lab} \leqslant 33^\circ$) to backward ($120^\circ \leqslant \theta_{\rm lab} \leqslant 166^\circ$) yield ratios for $Z =$ 1–4 fragments under various gating conditions for the 200-MeV $p +$ Ag reaction.

	$Z =$	1	2	3	4
Backward proton ($E_p > 20$ MeV, $147^\circ \leqslant \theta_{\rm lab} \leqslant 166^\circ$)		4.0	2.7	8.0	6.0
Backward proton ($9 \leqslant E_p \leqslant 12$ MeV, $147^\circ \leqslant \theta_{\rm lab} \leqslant 166^\circ$)		3.3	2.4	5.7	6.8
All events (ungated)		2.3	2.0	4.6	3.9
Forward proton ($E_p > 20$ MeV; $33^\circ \leqslant \theta_{\rm lab} \leqslant 52^\circ$)		2.1	1.8	3.8	3.7

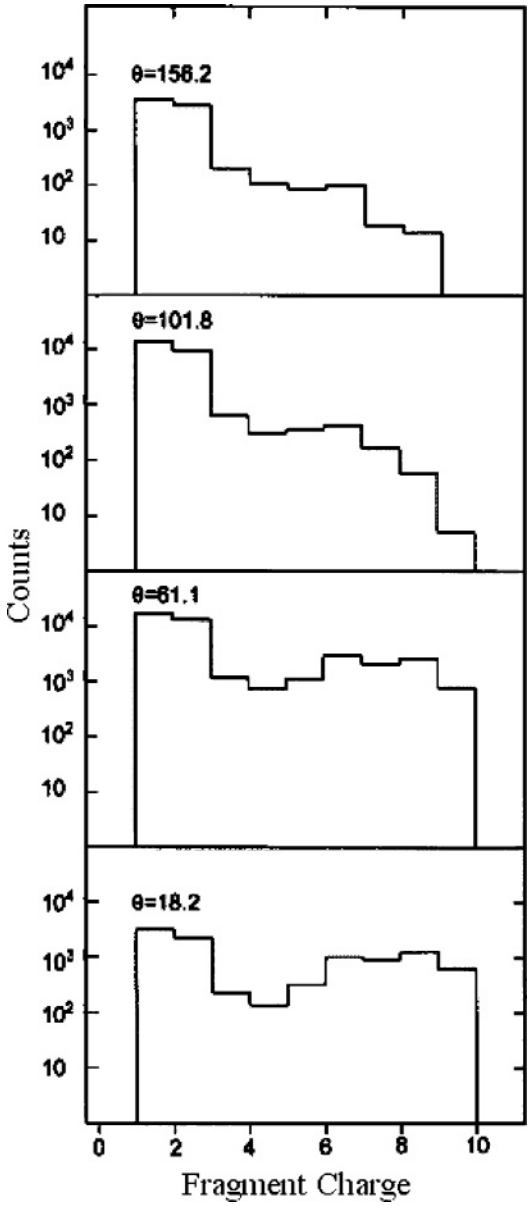

FIG. 13. Fragment charge distributions measured at (progressing clockwise from upper left) lab angles of 16, 61, 102, and 156 degrees for 200-MeV $p + {}^{27}$Al events with $12 \geqslant Z_{\rm obs} \geqslant 14$.

events at angles k, l. Because of the low probability for IMF-IMF pairs, we have gated on one He nucleus and one IMF; energy gates have also been imposed to separate thermal-like from pre-equilibrium fragments. For the ^{27}Al target, the maximum in the correlation function is near 180°, with the energetic fragments correlated more strongly. Since the charge of the two fragments comprises a significant fraction of the total available charge, this observation seems consistent with fission-like emission dominated by the Coulomb field of the system. Comparison with N-body breakup [39] simulations indicate a time scale of ∼200 fm/c for the ^{27}Al system.

For the silver target, the results are quite different. The correlation function for the more energetic component of the spectrum is nearly independent of opening angle, with a slight preference for backward angles. This behavior suggests a significant difference in the emission time of the two fragments, so that the second fragment is unperturbed by its predecessor. For the soft component, however, the correlation function strongly favors small opening angles. This may be in part due to the α-Li breakup channels in ^{10,11}B, but even with Li fragments gated out, the effect persists. Thus, these correlation studies further support a time-dependent reaction mechanism controlled largely by Coulomb effects, momentum conservation and phase space considerations.

4. Summary

Exclusive observables for the 200-MeV $p+{}^{27}$Al and $^{\rm nat}$Ag and 130 and 270 MeV ^{3}He + $^{\rm nat}$Ag and ^{197}Au systems have been measured. As in previous studies at these energies, preequilibrium and equilibrium emission mechanisms provide a consistent interpretation of the data. The ungated observables agree qualitatively with those from previous inclusive measurements, and thus lend themselves to analysis in the context of a multi-source emission formalism. These observables include forward-peaked ejectile spectra with strong preequilibrium tails, statistical-like fragment distributions at backward angles, and ^{3}He-to-^{4}He ratios that increase rapidly with increasing fragment energy.

Analysis of exclusive observables shows a systematic dependence of charged-particle multiplicity on bombarding energy and target type. Furthermore, it is found that IMF coincidence gates can be used to select on higher or lower average multiplicities, and that this sensitivity is linked strongly to energy conservation considerations. In the most violent $p+{}^{27}$Al events event-by-event linear momentum distributions, as well as the angular dependence of fragment charge distributions, are consistent with large linear momentum transfers. Both linear momentum and transverse momentum distributions associated with preequilibrium fragment formation in $p + {}^{\rm nat}$Ag events argue for a time-dependent emission scenario, followed by statistical decay. Finally, angular yield ratios have also been found to depend on the choice of various coincidence gates.

In summary, these exclusive studies strengthen previous interpretations that suggest complex fragment emission in light-ion-reduced reactions is a time-dependent process dominated by statistical effects, the Coulomb field of the system and momentum conservation considerations. It is suggested that nonequilibrium fragments appear to have their origin in a hot, localized region of the nucleus that exists early in the energy dissipation process. This localized region of high temperature, combined with collective Fermi motion effects, seem essential to explain the high energy tails of the spectra at very forward angles. However, the cooling effect of nonequilibrium fragment emission leaves the residue in a much lower state of excitation, so that subsequent emissions are largely thermal in character. Thus, while the present data form a macroscopic picture of the reaction dynamics, they fail to enhance our understanding of fast fragment formation. It appears that experiments that emphasize the forwardmost spectra with significantly enhanced statistics, isotope resolution and neutron-emission information will be required to attack this problem in greater depth.

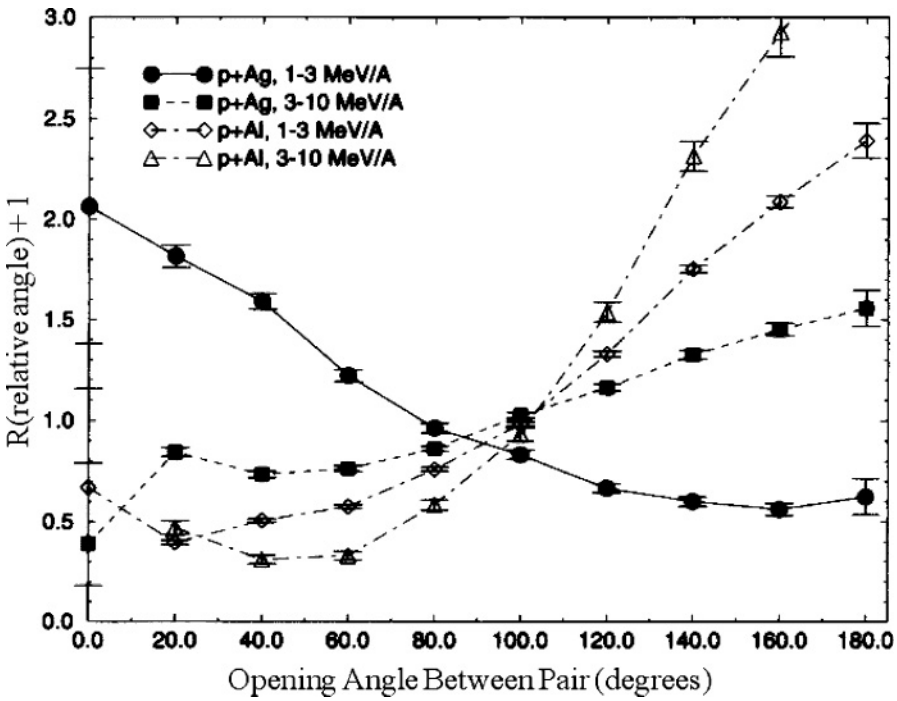

FIG. 14. Relative-angle correlation functions for fragment pairs with $Z \geqslant 2$ as a function of opening angle. Data are for 200-MeV $p + {}^{27}$Al (open points) and ^{nat}Ag (solid points), gated on fragment energy, as indicated on figure.

ACKNOWLEDGMENTS

The authors wish to thank Gary East and the IUCF operating crew for providing the beams for this study. Valuable assistance in conducting these experiments was provided by Dick Yoder, Bill Lozowski, John Vanderwerp and Kevin Komisarcik. This research was supported by the U.S. Department of Energy and U.S. National Science Foundation and the National Sciences and Engineering Research Council of Canada.

[1] R. E. L. Green and R. G. Korteling, Phys. Rev. C **22**, 1594 (1980); R. E. L. Green *et al.*, *ibid.* **29**, 1086 (1984).
[2] W. G. Lynch, Annu. Rev. Nucl. Part. Sci. **37**, 493 (1987).
[3] J. L. Wile *et al.*, Phys. Rev. C **45**, 2300 (1992).
[4] S. J. Yennello, K. Kwiatkowski, S. Rose, L. W. Woo, S. H. Zhou, and V. E. Viola, Phys. Rev. C **41**, 79 (1990).
[5] E. Renshaw, S. J. Yennello, K. Kwiatkowski, R. Płaneta, L. W. Woo, and V. E. Viola, Phys. Rev. C **44**, 2618 (1991).
[6] L. G. Sobotka *et al.*, Phys. Rev. Lett. **51**, 2187 (1983).
[7] M. A. McMahan, L. G. Moretto, M. L. Padgett, G. J. Wozniak, L. G. Sobotka, and M. G. Mustafa, Phys. Rev. Lett. **54**, 1995 (1985).
[8] L. G. Moretto, Nucl. Phys. **A247**, 211 (1975).
[9] J. Gomez del Campo, J. L. Charvet, A. DOnofrio, R. L. Auble, J. R. Beene, M. L. Halbert, and H. J. Kim, Phys. Rev. Lett. **61**, 290 (1988).
[10] V. E. Viola, K. Kwiatkowski, J. B. Natowitz, and S. J. Yennello, Phys. Rev. Lett. **93**, 132701 (2004).
[11] L. Beaulieu *et al.*, Phys. Rev. Lett. **84**, 5971 (2000).
[12] Y. Yariv, S. J. Yennello, K. Kwiatkowski, S. Rose, L. W. Woo, S. H. Zhou, and V. E. Viola, Phys. Rev. C **41**, 79 (1990).
[13] J. Cugnon, T. Mizutani, and J. Vandermuelen, Nucl. Phys. **A352**, 505 (1981); J. Cugnon, *ibid.* **A462**, 751 (1987).
[14] V. Toneev, N. S. Amelin, K. K. Gudima, and S. Y. Sivoklokow, Nucl. Phys. **A519**, 463c (1990).
[15] P. Danielewicz and G. F. Bertsch, Nucl. Phys. **A533**, 712 (1991); P. Danielewicz, Phys. Rev. C **51**, 716 (1995).
[16] S. Turbide, P. Danielewicz *et al.*, Phys. Rev. C **70**, 014608 (2004).
[17] J. P. Bondorf, A. S. Botvina, A. S. Iljinov, I. N. Mishustin, and K. Sneppen, Phys. Rep. **257**, 133 (1995).
[18] W. A. Friedman, Phys. Rev. C **42**, 667 (1990).
[19] D. H. E. Gross, Rep. Prog. Phys. **53**, 605 (1990).
[20] M. Blann, Annu. Rev. Nucl. Sci. **25**, 123 (1975); Phys. Rev. C **54**, 1341 (1996).
[21] E. Gadioli and P. E. Hodgson, Pep. Prog. Phys. **52**, 247 (1989).
[22] M. B. Chadwick and P. Oblozinsk, Phys. Rev. C **46**, 2028 (1992).
[23] R. Bond, P. J. Johansen, S. E. Koonin, and S. Garpman, Phys. Lett. **B71**, 43 (1977).
[24] D. H. Boal, R. E. L. Green, R. G. Korteling, and M. Soroushian, Phys. Rev. C **23**, 2788 (1981); **28**, 2568 (1983).
[25] D. J. Fields, W. G. Lynch, C. B. Chitwood, C. K. Gelbke, M. B. Tsang, H. Utsunomiya, and J. Aichelin, Phys. Rev. C **30**, 1912 (1984).
[26] K. Kwiatkowski *et al.*, Phys. Lett. **B171**, 41 (1986).
[27] K. Kwiatkowski *et al.*, Nucl. Instrum. Methods Phys. Res. A **360**, 571 (1995).
[28] W. G. Meyer, Ph.D. thesis, University of Maryland, 1975.
[29] D. Horn *et al.*, Nucl. Instrum. Methods A **320**, 273 (1992).
[30] F. Benrachi *et al.*, Nucl. Instrum. Methods A **281**, 137 (1989).
[31] T. Lefort *et al.*, Phys. Rev. C **64**, 064603 (2001).
[32] M. Fatyga *et al.*, Phys. Rev. Lett. **58**, 2527 (1987).
[33] D. E. Fields *et al.*, Phys. Lett. **B220**, 356 (1989).

[34] W. Skulski *et al*., Phys. Lett. **B218**, 7 (1989); W. Skulski, M. Fatyga, H. J. Karwowski, K. Kwiatkowski, V. E. Viola, K. Hicks, and R. Ristinen, Phys. Rev. C **40**, 1279 (1989).
[35] F. Zhu *et al*., Phys. Rev. C **44**, R582 (1991).
[36] K. Kwiatkowski, *et al*. Phys. Lett. **B423**, 21 (1998).
[37] J. R. Wu, C. C. Chang, and H. D. Holmgren, Phys. Rev. C **19**, 370 (1979); **19**, 659 (1979).
[38] R. Wada *et al*. Phys. Rev. Lett. **58**, 1829 (1987).
[39] T. Glasmacher *et al*., Phys. Rev. C **50**, 952 (1994).